HHS Public Access

Author manuscript

Int J Radiat Oncol Biol Phys. Author manuscript; available in PMC 2024 April 22.

Published in final edited form as:

Int J Radiat Oncol Biol Phys. 2022 July 01; 113(3): 614–623. doi:10.1016/j.ijrobp.2022.02.020.

Neuroprotective Effects of Ultra-High Dose Rate FLASH Bragg Peak Proton Irradiation

Ivana Dokic[*,†,‡,§,‖], **Sarah Meister**[*,†,‡,§,‖,¶], **Jovana Bojcevski**[*,†,‡,§,‖], **Thomas Tessonnier**[‖], **Dietrich Walsh**[*,†,‡,§,‖], **Maximilian Knoll**[*,†,‡,§,‖], **Stewart Mein**[*,†,‡,§,‖], **Zili Tang**[*,†,‡,§,‖], **Lena Vogelbacher**[*,†,‡,§,‖], **Claudia Rittmueller**[*,†,‡,§,‖], **Mahmoud Moustafa**[*,†,‡,§,‖,#], **Damir Krunic**[**], **Stephan Brons**[‖], **Thomas Haberer**[‖], **Jürgen Debus**[*,†,‡,§,‖], **Andrea Mairani**[‖,††], **Amir Abdollahi**[*,†,‡,§,‖]

[*]Clinical Cooperation Unit Translational Radiation Oncology, National Center for Tumor Diseases (NCT), Heidelberg University Hospital (UKHD) and German Cancer Research Center (DKFZ), Heidelberg, Germany

[†]Division of Molecular and Translational Radiation Oncology, Department of Radiation Oncology, Heidelberg Faculty of Medicine (MFHD) and Heidelberg University Hospital (UKHD), Heidelberg Ion-Beam Therapy Center (HIT), Heidelberg, Germany

[‡]German Cancer Consortium (DKTK) Core-Center Heidelberg, German Cancer Research Center (DKFZ), Heidelberg, Germany

[§]Heidelberg Institute of Radiation Oncology (HIRO), National Center for Radiation Oncology (NCRO), Heidelberg University and German Cancer Research Center (DKFZ), Heidelberg, Germany

[‖]Heidelberg Ion-Beam Therapy Center (HIT), Heidelberg, Germany

[¶]Faculty of Biosciences, Heidelberg University, Heidelberg, Germany

[#]Department of Clinical Pathology, Suez Canal University, Ismailia, Egypt

[**]Light Microscopy Facility, German Cancer Research Center (DKFZ), Heidelberg, Germany

[††]National Center for Oncological Hadrontherapy (CNAO), Pavia, Italy

Abstract

Purpose: To investigate brain tissue response to ultra-high dose rate (uHDR, FLASH) and standard dose rate (SDR) proton irradiations in the Bragg peak region.

Corresponding author: Ivana Dokic, PhD; i.dokic@dkfz.de.

Disclosures: J.D. reports grants from CRI – The Clinical Research Institute, GmbH grants from View Ray Inc, grants from Accuray International Sarl, grants from Accuray Incorporated, grants from RaySearch Laboratories AB, grants from Vision RT Ltd, grants from Merck Serono GmbH, grants from Astellas Pharma GmbH, grants from Astra Zeneca GmbH, grants from Siemens Healthcare GmbH, grants from Merck KGaA accounts payable, grants from Solution Akademie GmbH, grants from Ergomed PLC Surrey Research Park, grants from Siemens Healthcare GmbH, grants from Quintiles GmbH, grants from Pharmaceutecal Research Associates GmbH, grants from Boehringer Ingelheim Pharma GmbH Co, and grants from PTW-Freiburg, Dr Pychlau GmbH. A.A. report grants and other from Merck and EMD, grants and other from Fibrogen, other from BMS, other from BioMedX, and other from Roche outside the submitted work.

Methods and Materials: Active scanning uHDR delivery was established for proton beams for investigation of dose rate effects between clinical SDR and uHDR at ~10 Gy in the Bragg peak region (dose-averaged linear energy transfer [LET_D] ranging from 4.5 to 10.2 keV μm^{-1}). Radiation-induced injury of neuronal tissue was assessed by studying the DNA double strand break repair kinetics surrogated by nuclear γH2AX staining (radiation induced foci [RIF]), microvascular density and structural integrity (MVD, CD31+ endothelium), and inflammatory microenvironmental response (CD68+ microglia/macrophages and high mobility group box protein 1[HMGB]) in healthy C57BL/6 mouse brains.

Results: Averaged dose rates achieved were 0.17 Gy/s (SDR) and 120 Gy/s (uHDR). The fraction of RIF-positive cells increased after SDR ~10-fold, whereas a significantly lower fraction of RIF-positive cells was found after uHDR versus SDR (~2 fold, $P < .0001$). Moreover, uHDR substantially preserved the microvascular architecture and reduced microglia/macrophage regulated associated inflammation as compared with SDR.

Conclusions: The feasibility of uHDR raster scanning proton irradiation is demonstrated to elicit FLASH sparing neuroprotective effects compared to SDR in a preclinical *in vivo* model.

Introduction

Irradiation with ultra-high dose rates (uHDR, FLASH >35 Gy/s) has reemerged as a promising therapeutic tool, improving the normal tissue sparing while potentially maintaining tumor control. This effect has been seen mostly with electron beams and more recently with proton beams.[1]

FLASH investigations, focused on dosimetry and bioeffect observations using proton beams, have mainly involved laser acceleration and passive scattering delivery (PSD). Adaptation of clinical accelerators is underway to provide proton FLASH radiation therapy, mostly using PSD and beam modifiers; for example, ridge filter[2] to effectively deliver uHDR spread-out Bragg peaks (SOBP) using single energy layers. In vivo investigations available in literature for uHDR proton beams mainly focus on the normal tissue (skin and gastrointestinal tract)[1,3,4] and tumor response studies[5] at the entrance region of the Bragg peak. Whereas a few studies describe protective effects of uHDR in the brain tissue using electrons,[6,7] brain normal tissue response to uHDR proton Bragg peak region is completely missing. To address this, we focused on healthy mouse brain response to standard dose rate (SDR) and uHDR proton Bragg peak region in terms of DNA damage and radiation injury of brain microenvironment (CD31/PECAM-1 and CD68 expression). DNA damage was assessed by the analysis of the classical DNA double-strand break (DSB) surrogate marker, H2AX phosphorylated on serine 139 (γH2AX),[8] and brain microvasculature stability was investigated using platelet endothelial cell adhesion molecule −1 (PECAM-1 or CD31). CD31 is expressed on cells of the vascular compartment and regulates vascular integrity and immune cell trafficking.[9] The expression of CD31 can be used as a surrogate to describe stability of endothelium and blood-brain barrier (BBB).[10] Loss of BBB/endothelium integrity, represented as a decrease in CD31 signal, may be used as a readout of an irradiation injury in vivo.[11,12]

Microglia, often called resident brain macrophages, are an important regulator of brain innate immunity, brain inflammation, and injury.[13,14] As a consequence of brain injury, such as radiation-induced brain injury, microglia/macrophages upregulate expression of transmembrane glycoprotein CD68 and switch from resting to reactive state.[15,16] High mobility group box protein 1 (HMGB1) is a nuclear protein that regulates DNA and chromatin architecture in healthy cells.[17] HMGB1 is actively released upon inflammation in innate immune cells[18,19] and is passively released from the nucleus to cytoplasm of dying cells, which can be used as a marker of necrosis[20] and senescence.[21] Upon brain injury, HMGB1 is released from dying neurons and can promote immune activation of glial cells.[22]

In this work, we present the first evidence of healthy brain tissue sparing for proton beam FLASH dose rate in the Bragg peak region.

Methods and Materials

Planning and irradiation

Treatment plans were generated to consist of 9 spots (3 mm separation, 6 × 6 mm^2) to deliver 10 Gy in the center of each brain (~3.9 mm below the skin) for a depth-wise peak width of ~3 mm, for both SDR and uHDR (FLASH) irradiations with 146.6 MeV/u proton beams (full width at half maximum (FWHM): 1 cm). The total number of particles used was 7.6E + 9. A collimator (material: PMMA [polymethylmethacrylat]; thickness 1 cm; aperture: 6 × 6 mm^2) was placed on top of the mouse heads, with a 2.5cm air gap after a 122mm PMMA range shifter. The collimator helped to enhance target precision for small volumes, resulting in an iso-line above 90% of the planned dose of 4 × 4 mm^2. We verified field size with EBT3 gafchromic films with and without collimator. Additional measurements with collimator were performed to assure that the measured dose was within ±5% of the desired dose level.

For conventional irradiations, the delivery of the mono-energetic layer was divided into 10 spills to achieve an average dose rate closer to clinical scenarios (0.17 Gy/s). As summarized in Table 1, for the 10 spills separated by about 6.5 seconds from each other (interspill time), the accelerating system delivered 1 Gy to each mouse in 250 ms (spill time), for a total irradiation time of around 58 seconds (delivery time). For FLASH irradiations, the delivery of the 10 Gy was made in 1 spill ~80 ms (Table 1), achieving 120 Gy/s dose rate. Raster-scanning of the 9-spot plan was performed at ~9 ms/spot. For both cases, measurements with ionization chamber (PinPoint chamber 31015, PTW) following TRS398 were performed to verify the dose at the desired position. PinPoint chamber was cross-calibrated against a reference Farmer chamber, used clinically in our facility.

For delivery verification and physical distribution quantification, a detailed geometry of the in vivo experimental setup was incorporated into the in-house FLUKA Monte Carlo (MC) simulation system, including specifications of the Heidelberg Ion-Beam Therapy Center (HIT) beamline.[23,24] Simulations were performed for dose and dose-averaged linear energy transfer (LET_D) prediction (4 × 4 mm section in the beam's eye view). Additionally, MC simulations were performed with RayStation.

Animal model

The study animals were 6-week-old female C57BL/6 mice (Janvier Labs). For irradiation, the mice were anesthetized with isoflurane and fixed in custom holders. A collimator was placed over the head of each mouse, sparing an area of 6 × 6 mm^2 above the right hemisphere as irradiation field. For each treatment 5 mice were used (Ctrl = 5, SDR = 5, uHDR = 5) at each time point (1 hour and 7 days post-treatment). Animal work was performed according to rules approved by the local and governmental animal care committee instituted by the German government (Regierung-spraesidium, Karlsruhe).

Tissue preparation and immunofluorescence

At 1 hour and 7 days after irradiation, mice were anesthetized with 120 mg/kg ketamine (Ketaset; Zoetis) and 20 mg/kg xylazin (Rompun; Bayer) and transcardially perfused with ice-cold phosphate-buffered saline (PBS) (Gibco) followed by ice-cold 4% paraformaldehyde (Carl Roth) in PBS. The mice were decapitated and brains were fixed in 4% paraformaldehyde and cryoprotected with 30% sucrose (Roth) in PBS until they sank. Brains were placed in Tissue-Tek Cryomolds (Sakura Finetek) and embedded in Tissue-Tek O.C.T. Compound (Sakura Finetek) before slow freezing in isopentane (2-methylbutane; Honeywell; precooled in liquid nitrogen) and subsequent storage at −80°C. Brains were sagittally sectioned on a cryotome CryoStar NX70 (Thermo Scientific).

For immunofluorescence, brain sections were thawed at room temperature, washed, and blocked using blocking buffer containing 2.5% goat serum, 1% bovine serum albumine, and 0.1% Triton X in PBS and ReadyProbes Mouse-on-Mouse IgG Blocking Solution (Invitrogen) according to manufacturer's instructions. To visualize DNA damage, γH2AX antibody (1:100; CellBiolabs) was applied on 8-μm thick sections. For endothelial cell and blood vessel assessment, CD31 (1:50; Abcam) antibody was applied on 25-μm thick sections. For microglia/macrophage identification, CD68 antibody (1:100; Bioss antibodies) was used, and HMGB1 was visualized using an Abcam antibody (1:400) on 8-μm thick sections. Slides were washed and signals detected with secondary antibodies (1:400) coupled with Alexa Fluor 647 (γH2AX, HMGB1) or Alexa Fluor 555 (CD31, CD68) (Invitrogen). Specificity of staining was confirmed using negative controls where only secondary antibody was applied on the samples. DAPI (4',6-diamidino-2-phenylindole; 1:1000; Sigma-Aldrich) dye was used to stain nuclei.

Microscopy and image analysis

For image analysis and evaluation, samples were imaged with a microscope consisting of a Zeiss LSM780 with a Yokogawa CSU-W1 spinning disk system. Fluorescently labeled antibodies and DAPI signals were captured with constant laser power and exposure time. Regions of interest (ROIs) for CD31 stained blood vessels and nuclei images were captured as 16 bit images in a 3 × 3 tile structure in stacks of 5 with a z-interval of 2.5 μm. The γH2AX signal and nuclei were captured as 16-bit images in a 4 × 4 tile structure in stacks of 4 with a z-interval of 1 μm. Tile overlap was set to 5% in Zen Blue software (Zeiss).

For each ROI, image stack capture and maximum intensity z-projection were performed before being exported to a 16-bit tiff using Zeiss Zen Blue. The images were then analyzed

using the high throughput software ScanR Analysis (v3.2). For γH2AX, a nuclei detection based on DAPI intensity thresholding was performed followed by a subobject routine, which detected nuclear γH2AX signal above a defined fixed threshold based on the control nonirradiated samples. The resulting nuclei, which were positive for DAPI and γH2AX, were scored. For γH2AX nuclear signal total intensity analysis, total intensities within control samples were averaged and normalized to 1, and total intensity signals from the treated cells were normalized to the averaged control signal. The change in γH2AX total intensity signal was then expressed as a fold change in comparison to the control. For CD31 detection a thresholding and edge detection method was used to detect the CD31-positive blood vessels. The vessels were counted and divided into 3 categories based on elongation factor (0-3, small; 3-6, medium; 6-max, long). CD31+ microvascular density was calculated as the proportion of CD31+ signal area over the total measurement ROI area and expressed as a percentage.

A Zeiss Axio Scan.Z1 microscope equipped with a Colibri 5/7 with 385 nm, 567 nm, and 630 nm LEDs (light-emitting diodes), 20 × 0.8 Plan-Apo objective, and Orca Flash 4.0 V2 sCMOS camera was used for imaging CD68− and HMGB1-stained tissues. The complete sections with fluorescently labeled antibodies and DAPI signals were scanned automatically with constant LED power and exposure time. In these sections, nuclei detection and quantification were based on DAPI intensity thresholding, as well as CD68 signal. To quantify percentage of CD68-positive cells per image, CD68 signal was normalized to the number of nuclei. To quantify HMGB1 nuclear signal, DAPI-stained nuclei were segmented based on edge detection, and HMGB1 total intensity was measured within nuclei. HMGB1 nuclear total intensity signal within control samples was averaged and normalized to 1. HMGB1 total intensities from nuclei of the treated cells were normalized to the averaged control signal. The change in HMGB1 total intensity signal was then expressed as a fold change in comparison to the control. Representative images for all figures were acquired using the LSM700 confocal microscope with 20x objective, to assure the best possible resolution (1 px = 0.333 μm). For all images, analyses were performed in irradiated cortical brain area to keep the structural consistency of the investigated brain region among the samples.

Statistical analysis

For each treatment group, 5 mice were analyzed (Ctrl = 5, SDR = 5, uHDR = 5), at each time point (1 hour and 7 days posttreatment). Ten ROIs were analyzed for each tissue, and comparison between treatment outcomes was performed using GraphPad Prism software applying one-way analysis of variance (ANOVA) with Tukey's multiple comparisons test.

Results

Irradiation parameters

Both conventional and FLASH plans were successfully delivered. The average measured doses, spill times, interspill times, delivery times, and dose rates are reported in Table 1. MC simulation was verified by measured dose within ±3%. LET_D range between proximal and distal R_{80} (range at which dose is 80% of the maximum Bragg peak dose) was from 4.5 to

10.2 keV μm^{-1}. Profiles of dose and LET_D as function of depth within the mice brain are shown in Figure 1A.

Standard and ultra-high (FLASH) dose rate in vivo experimental approach

The photos and schematic for the animal SDR versus uHDR (FLASH) trial depict irradiation setup and methodology from irradiation delivery to analysis (Fig. 1B, 1C). Mice were irradiated using a clinical-like setting at our facility. They were positioned within a holder and anesthetized by isoflurane during irradiation, as depicted in Figure 1B. The isocenter was positioned at the upper right quadrant of the right hemisphere. The Bragg peak was delivered at about 4-mm depth in the mouse head. An MC calculation of the expected dose distribution of a previously performed computed tomography[25] is shown in Figure 1B, together with the implemented geometric setup (collimator, PMMA block, and air gap).

Experimental pipeline after irradiation includes the brain isolation and cryo-preservation (details in the Methods and Materials section) at various time points post-irradiation (1 hour and 7 days). After this, brains were sectioned (sagittally, as depicted in middle panel of Fig. 1C) and prepared for immunofluorescence staining and microscopy. The sagittal sectioning assured that the irradiated ROI was imaged and analyzed.

DNA damage response in mouse healthy brains after SDR versus uHDR

Irradiation at 10 Gy lead to an induction of H2AX phosphorylation 1 hour after SDR and uHDR irradiation and was characterized by pan nuclear γH2AX signal (Fig. 2A). When comparing SDR- to uHDR-induced γH2AX, uHDR presented a substantial, statistically significant reduction in γH2AX signal: a reduction in γH2AX-positive nuclei percentage as well as γH2AX total intensity (Fig. 2A). To examine residual DNA damage, we tested γH2AX formation at day 7 postirradiation and found ~2.5-fold reduction of the γH2AX-positive cell fraction after uHDR versus SDR. γH2AX signal intensity decreased to the background level after uHDR irradiation (Fig. 2B).

Brain microenvironment response after SDR versus FLASH radiation therapy

Figure 3A shows the brain microvascular endothelial CD31 signal in control samples, as well as after SDR and uHDR proton irradiation (7 days post-treatment), scored and grouped into 3 categories (short, medium, and long) based on their elongation factor (for details see Methods and Materials). Irradiation led to a decrease of CD31+ microvascular density. As demonstrated in Figure 3B, a protective effect using uHDR was found, presented in the more prevalent existence of CD31+ structures. This protective trend was observed for medium and long structures (Fig. 3B).

Considering infiltrative brain reactive (CD68+) microglia/macrophages, their presence in investigated cortical regions of the brain was relatively low (~4%). A 1.75-fold increase in CD68 signal was observed after SDR. In uHDR irradiated samples, CD68 expression remained similar to the one of control samples (Fig. 4). Brain cells damage and neuroinflammation were further assessed using HMGB1 as a marker.[19] In control cells, HMGB1 retained its nuclear localization, whereas in irradiated brains it relocated to cytoplasm (Fig. 5). This relocation was particularly apparent for SDR-irradiated brains (Fig.

5A). HMGB1 relocation to cytoplasm and consecutive decrease of its nuclear signal were quantified measuring HMGB1 nuclear signal total intensity, where the strongest decrease in nuclear HMGB1 was observed for the SDR group (Fig. 5B).

Discussion

Compared with SDR, uHDR (FLASH) electron irradiation has been shown to exhibit neuroprotective effects.[6,7] However, due to the limiting depth-dose distribution of electron beams, its clinical utilization is restricted to superficial tumors.[26] Treatment of deep-seated tumors requires precise and accurate delivery of high dose to the target, which is achievable with heavier charged particles, such as protons, helium, and carbon ions.[27,28] Therefore, we sought to investigate if pencil beam uHDR proton irradiation may also elicit similar FLASH sparing effects for the endpoint acute neurotoxicity. For this purpose, we established a platform for comparative studies with synchrotron-generated SDR and uHDR FLASH protons in a C57BL/6 mice in vivo brain model.

We report differential radiobiological effects of FLASH versus SDR proton irradiation on multiple layers, that is, DNA-damage and repair kinetics, microvascular architecture, and inflammatory response as surrogates for acute radiation toxicity of the normal mouse cortex. The data revealed significantly reduced fraction of γH2AX-positive cells 1 hour and 7 days post 10 Gy uHDR ~120 Gy/s versus SDR proton irradiation. Reduced γH2AX signal after uHDR irradiation at an early time point, which remained apparent for up to 7 days, could indicate differential double-strand breaks (DSB) damage formation and/or repair. DNA damage, and especially complex DSB, being a hallmark of radiation induced cytotoxicity,[29] may be directly linked to the tissue damage after SDR and uHDR irradiation, where the decreased DSB presence in uHDR tissues is directly responsible for the uHDR sparing effect. Even though biological mechanisms of the uHDR sparing effect are complex and not fully understood, reduced DNA damage by uHDR irradiation has been postulated, together with oxygen depletion theory, as one of the possible mechanisms of action (reviewed in Lin et al[30]). In this work, DNA damage reduction is indeed remarkable (~2-fold for both time points) compared with, for example, in vitro data available in the literature. Considering proton uHDR radiation therapy and especially γH2AX response, in vitro and in vivo data available in literature are sparse, mostly describing cell or tissue response in the entrance channel of the Bragg peak. For example, Buonanno et al[31] found no significant differences in γH2AX signal in normoxic condition in vitro for normal human lung fibroblast cells exposed to LET = 10 keV/μm protons delivered at 0.05, 100, or 1000 Gy/s for dose values up to 10 Gy. A reduction in γH2AX signal was found only for 20 Gy irradiation at 1000 Gy/s. Analogously, other recent works[32] using uHDR electron beam irradiation of fibroblasts in vitro at lower doses (<6 Gy) demonstrate no apparent difference in γH2AX. On the contrary, our experiment with proton beams in vivo indicates a decrease in γH2AX after uHDR irradiation compared with SDR, using the described physical parameters and settings in normal brain tissue. In line with the data presented here, the uHDR sparing effect for proton irradiation was recently reported by Cunningham et al,[4] where 35 Gy protons at ~115 Gy/s efficiently led to decreased skin and soft tissue toxicity in vivo. Similarly, a sparing effect of 15 Gy protons on intestinal tissue has been demonstrated by Diffenderfer et al[3] for the entrance region of the Bragg peak at ~78 Gy/s and Kim et al[33] for the spread-out

Bragg peak region at ~108 Gy/s. The lack of the sparing effect in vitro, in normoxic conditions, compared with in vivo data could be explained by the complexities of the tissue structure and the role of different tissue oxygen levels and tissue microenvironment.[34]

In regards to tissue microenvironment and radiation-induced brain injury, we observed sparing of microvasculature density architecture when FLASH irradiation was applied. Although proton SDR led to a decrease of CD31-positive vessels, an effect previously described in different models for proton and heavier carbon irradiation,[25,35] uHDR protected brain microvessel architecture. In line with our findings, similar sparing effects on CD31+ microvessels in vivo were reported for uHDR electron irradiation, using 15 Gy dose at ~350 Gy/s for uHDR and ~0.06 Gy/s for SDR.[36] Another aspect of radiation-induced brain injury is neuroinflammation, often mediated through brain-activated microglia/macrophages. Studies with x-rays,[37] as well as more recent work with helium beams, indicated an increase in CD68 signal after irradiation in mouse brains.[38] Accordingly, we observed an increase in CD68-positive cells after proton SDR but not uHDR irradiation. In the same line, investigation of HMGB1 molecule expression in brain tissue indicated nuclear release of HMGB1 in irradiated samples, which was particularly apparent for SDR-treated brains. FLASH irradiated brains exhibited HMGB1 nuclear release to a lower extent compared with SDR irradiation. Nuclear release of HMGB1 has been linked to the increased neuroinflammation upon inflammasome activation,[22] and it is a characteristic of necrotic, dying, and senescent cells.[19-21] HMGB1 release leads to microglia activation, which then mediates neuroinflammation and neuronal damage.[39] HMGB1-mediated inflammation can then contribute to endothelium damage and eventually BBB disruption.[16,40]

To our knowledge, this is the first proof-of-concept report demonstrating neuroprotective effects of FLASH proton irradiation in vivo. Longer prospective follow-up studies are required to investigate if the FLASH sparing effects of uHDR protons also translate to attenuation of late radiation-induced neurotoxicity. Additionally, the effects of beam delivery parameters, such as instantaneous dose rate, pulse number, pulse-to-pulse interval, and fractionation scheme (one vs few fractions), still need to be quantified to understand the full potential of the observed FLASH neuroprotective effects for clinical applications.

Conclusions

Together, this work demonstrates the feasibility of uHDR raster scanning proton irradiation to elicit FLASH sparing neuroprotective effects in the Bragg peak compared with SDR in a preclinical in vivo model. Moreover, this study opens possibilities for further exploration of the high dose rate effect in particle therapy with possible benefit for clinical translation, for example, for reduction of normal tissue toxicities in the Bragg peak region close to the tumor target volume.

Acknowledgments

The authors thank the HIT accelerator team for establishing and providing the FLASH ion beam.

This work was supported by intramural funds from the National Center for Tumor diseases (NCT3.0_2015.21/22 NCT-PRO and Biodose programs) and German Cancer Consortium (DKTK) and in part by the collaborative research center of the German research foundation (DFG, Unite, SFB-1389, project number 404521405). This work

was supported in part by NIH-1P01CA257904-01A1. The funders had no role in study design, data collection and analysis, decision to publish, or preparation of the article.

Data sharing statement:

Research data are stored in an institutional repository and will be shared upon request to the corresponding author.

References

1. Wilson JD, Hammond EM, Higgins GS, Petersson K. Ultra-high dose rate (FLASH) radiotherapy: Silver bullet or fool's gold? Front Oncol 2019;9:1563. [PubMed: 32010633]
2. Patriarca A, Fouillade C, Auger M, et al. Experimental set-up for FLASH proton irradiation of small animals using a clinical system. Int J Radiat Oncol Biol Phys 2018;102:619–626. [PubMed: 30017793]
3. Diffenderfer ES, Verginadis II, Kim MM, et al. Design, implementation, and in vivo validation of a novel proton FLASH radiation therapy system. Int J Radiat Oncol Biol Phys 2020;106:440–448. [PubMed: 31928642]
4. Cunningham S, McCauley S, Vairamani K, et al. FLASH proton pencil beam scanning irradiation minimizes radiation-induced leg contracture and skin toxicity in mice. Cancers (Basel) 2021;13:1012. [PubMed: 33804336]
5. Rao R, Ogurek S, Sertorio M, et al. Comparison of FLASH vs conventional dose rate proton radiation in endogenous mouse brain tumor model. Int J Radiat Oncol Biol Phys 2020;108:E742.
6. Montay-Gruel P, Acharya MM, Petersson K, et al. Long-term neurocognitive benefits of FLASH radiotherapy driven by reduced reactive oxygen species. Proc Natl Acad Sci USA. 2019;116:10943–10951. [PubMed: 31097580]
7. Montay-Gruel P, Markarian M, Allen BD, et al. Ultra-high-dose-rate FLASH irradiation limits reactive gliosis in the brain. Radiat Res 2020;194:636–645. [PubMed: 32853387]
8. Rogakou EP, Pilch DR, Orr AH, Ivanova VS, Bonner WM. DNA double-stranded breaks induce histone H2AX phosphorylation on serine 139. J Biol Chem 1998;273:5858–5868. [PubMed: 9488723]
9. Newman PJ, Berndt MC, Gorski J, et al. PECAM-1 (CD31) cloning and relation to adhesion molecules of the immunoglobulin gene superfamily. Science 1990;247:1219–1222. [PubMed: 1690453]
10. Lertkiatmongkol P, Liao D, Mei H, Hy Y, Newman PJ. Endothelial functions of platelet/endothelial cell adhesion molecule-1 (CD31). Curr Opin Hematol 2016;23:253–259. [PubMed: 27055047]
11. Wimmer I, Tietz S, Nishihara H, et al. PECAM-1 stabilizes blood-brain barrier integrity and favors paracellular T-cell diapedesis across the blood-brain barrier during neuroinflammation. Front Immunol 2019;10:711. [PubMed: 31024547]
12. Grabham P, Sharma P. Acute effects of ionizing radiation on human endothelial barrier function. J Radiat Res 2014;55(suppl_1):i97–i98.
13. Nimmerjahn A, Kirchhoff F, Helmchen F. Resting microglial cells are highly dynamic surveillants of brain parenchyma in vivo. Science 2005;308:1314–1318. [PubMed: 15831717]
14. Hanisch UK, Microglia Kettenmann H. Active sensor and versatile effector cells in the normal and pathologic brain. Nat Neurosci 2007;10:1387–1394. [PubMed: 17965659]
15. Walker DG, Lue LF. Immune phenotypes of microglia in human neurodegenerative disease: Challenges to detecting microglial polarization in human brains. Alzheimers Res Ther 2015;7:56. [PubMed: 26286145]
16. Lumniczky K, Szatmari T, Safrany G. Ionizing radiation-induced immune and inflammatory reactions in the brain. Front Immunol 2017;8:517. [PubMed: 28529513]
17. Baxevanis AD, Landsman D. The HMG-1 box protein family: Classification and functional relationships. Nucleic Acids Res 1995;23:1604–1613. [PubMed: 7784217]

18. Andersson U, Tracey KJ. HMGB1 is a therapeutic target for sterile inflammation and infection. Annu Rev Immunol 2011;29:139–162. [PubMed: 21219181]
19. Scaffidi P, Misteli T, Bianchi ME. Release of chromatin protein HMGB1 by necrotic cells triggers inflammation. Nature 2002;418:191–195. [PubMed: 12110890]
20. Raucci A, Palumbo R, Bianchi ME. HMGB1: A signal of necrosis. Autoimmunity 2007;40:285–289. [PubMed: 17516211]
21. Davalos AR, Kawahara M, Malhotra GK, et al. p53-dependent release of Alarmin HMGB1 is a central mediator of senescent phenotypes. J Cell Biol 2013;201:613–629. [PubMed: 23649808]
22. Kim JB, Choi JS, Yu Y-M, et al. HMGB1, a novel cytokine-like mediator linking acute neuronal death and delayed neuroinflammation in the postischemic brain. J Neurosci 2006;26:6413–6421. [PubMed: 16775128]
23. Parodi K, Mairani A, Brons S, et al. Monte Carlo simulations to support start-up and treatment planning of scanned proton and carbon ion therapy at a synchrotron-based facility. Phys Med Biol 2012;57: 3759–3784. [PubMed: 22617050]
24. Mairani A, Bohlen TT, Schiavi A, et al. A Monte Carlo-based treatment planning tool for proton therapy. Phys Med Biol 2013;58:2471–2490. [PubMed: 23514837]
25. Chiblak S, Tang Z, Lemke D, et al. Carbon irradiation overcomes glioma radioresistance by eradicating stem cells and forming an antiangiogenic and immunopermissive niche. JCI Insight 2019;4.
26. Baskar R, Lee KA, Yeo R, Yeoh K-W. Cancer and radiation therapy: Current advances and future directions. Int J Med Sci 2012;9:193–199. [PubMed: 22408567]
27. Loeffler JS, Smith AR, Suit HD. The potential role of proton beams in radiation oncology. Semin Oncol 1997;24:686–695. [PubMed: 9422264]
28. Jakel O. Physical advantages of particles: Protons and light ions. Br J Radiol 2020;93 20190428. [PubMed: 31556333]
29. Mavragani IV, Nikitaki Z, Souli MP, et al. Complex DNA damage: A route to radiation-induced genomic instability and carcinogenesis. Cancers (Basel) 2017;9.
30. Lin B, Gao F, Yang Y, et al. FLASH radiotherapy: History and future. Front Oncol 2021;11:644400. [PubMed: 34113566]
31. Buonanno M, Grilj V, Brenner DJ. Biological effects in normal cells exposed to FLASH dose rate protons. Radiother Oncol 2019;139:51–55. [PubMed: 30850209]
32. Fouillade C, Curras-Alonso S, Giuranno L, et al. FLASH irradiation spares lung progenitor cells and limits the incidence of radio-induced senescence. Clin Cancer Res 2020;26:1497–1506. [PubMed: 31796518]
33. Kim MM, Verginadis II, Goia D, et al. Comparison of FLASH proton entrance and the spread-out Bragg peak dose regions in the sparing of mouse intestinal crypts and in a pancreatic tumor model. Cancers (Basel) 2021;13.
34. Marcu LG, Bezak V, Peukert DD, Wilson P. Translational research in FLASH radiotherapy-from radiobiological mechanisms to in vivo results. Biomedicines 2021;9:181. [PubMed: 33670409]
35. Jang GH, Ha J-H, Huh T-L, Lee YM. Effect of proton beam on blood vessel formation in early developing zebrafish (Danio rerio) embryos. Arch Pharm Res 2008;31:779–785. [PubMed: 18563361]
36. Kim YE, Gwak S-H, Hong B-J, et al. Effects of ultra-high dose rate FLASH irradiation on the tumor microenvironment in Lewis lung carcinoma: Role of myosin light chain. Int J Radiat Oncol Biol Phys 2021;109:1440–1453. [PubMed: 33186615]
37. Xue J, Dong J-H, Huang G-D, et al. NF-kappaB signaling modulates radiation induced microglial activation. Oncol Rep 2014;31:2555–2560. [PubMed: 24756575]
38. Allen BD, Syage AR, Maroso M, et al. Mitigation of helium irradiation-induced brain injury by microglia depletion. J Neuroinflammation 2020;17:159. [PubMed: 32429943]
39. Gao HM, Zhou H, Zhang F, et al. HMGB1 acts on microglia Mac1 to mediate chronic neuroinflammation that drives progressive neurodegeneration. J Neurosci 2011;31:1081–1092. [PubMed: 21248133]

40. Fiuza C, Bustin M, Talwar S, et al. Inflammation-promoting activity of HMGB1 on human microvascular endothelial cells. Blood 2003;101:2652–2660. [PubMed: 12456506]

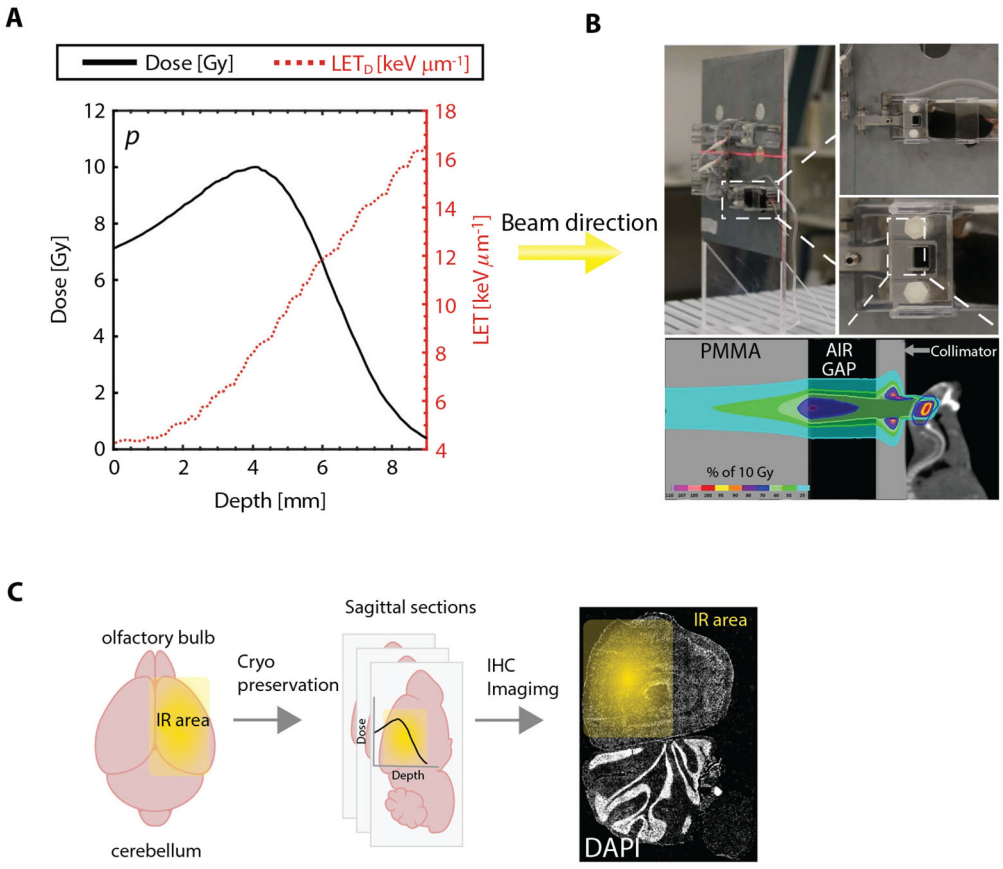

Fig. 1.

(A) Central profiles for depth dose (black solid line) and dose-averaged linear energy transfer ($LET_{D;}$ red dotted line) for both standard dose rate and FLASH proton plan irradiations ($D_{max} \simeq 10$ Gy) with Bragg peak position of ~4 mm depth. (B) Image representations of mouse positioning during IR. A Monte Carlo calculation of the expected dose distribution overlaid on a mouse computed tomography scan is shown together with the implemented geometric setup (collimator, PMMA block, and air gap). The mouse brain is delineated with a blue line. (C) Experimental pipeline scheme includingIR field position (right hemisphere). *Abbreviations:* DAPI = 4',6-diamidino-2-phenylindole; IHC = immunohistochemistry; IR = irradiation; LET_D = dose-averaged linear energy transfer; PMMA = polymethylmethacrylate.

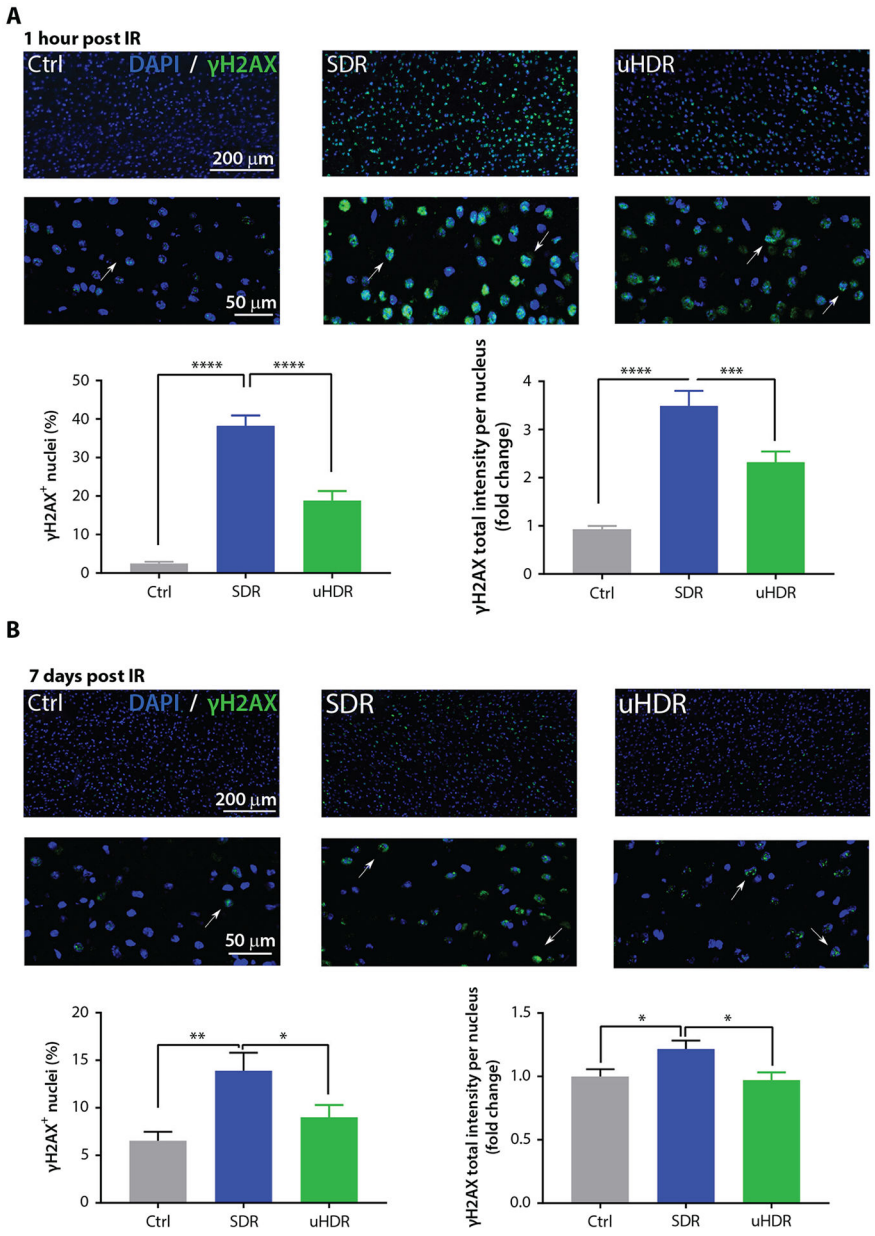

Fig. 2.

Standard dose rate (SDR) versus ultra-high dose rate (uHDR) irradiation effects on pS139 H2AX foci (γH2AX) formation. Representative images and quantification of γH2AX positive nuclei at 1 hour (A; Ctrl = 5, SDR = 5, uHDR = 5, brains) and 7 days (B; Ctrl = 5, SDR = 5, uHDR = 5, brains) post-irradiation of healthy C57BL/6 mouse brain sections after SDR and uHDR (magnification 20 ×). Arrows point to the γH2AX positive nuclei. For analysis we used n = 10 regions of interest per tissue section; n > 3000 nuclei per condition. Treatments were compared using analysis of variance (ANOVA) Tukey's post hoc test, standard error of the means (SEM) (***$P < .005$, ****$P < .0001$).

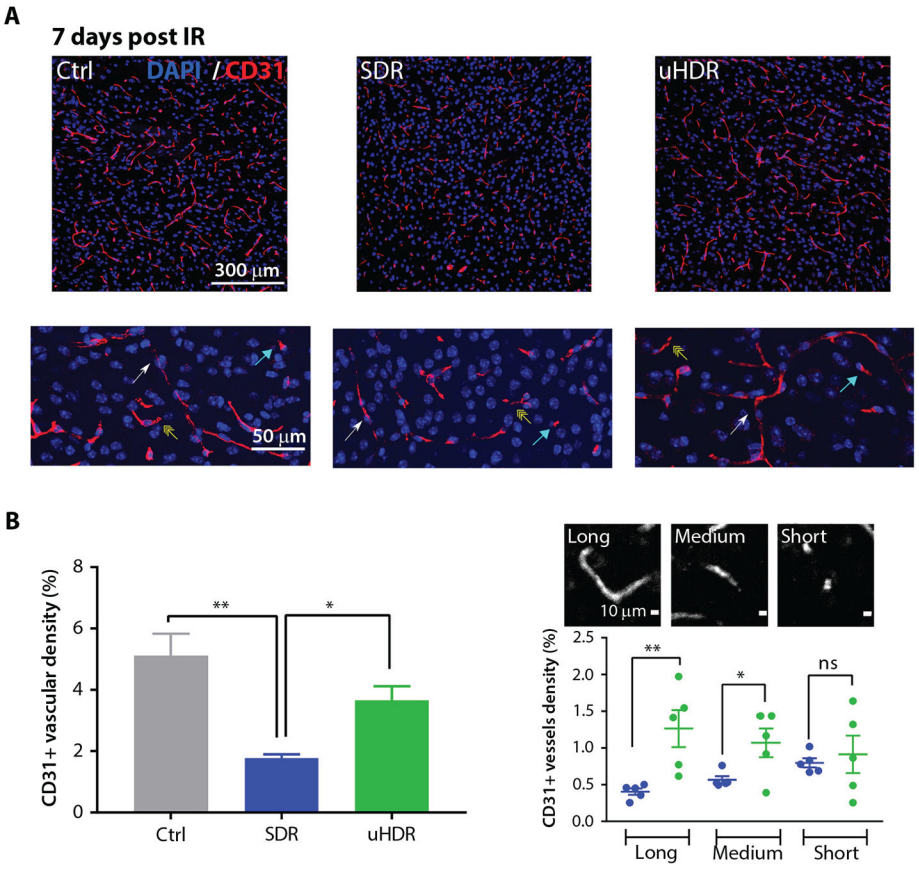

Fig. 3.

Standard dose rate (SDR) versus ultra-high dose rate (uHDR) effects on brain microvascular architecture. (A) Representative images (magnification 20 ×). Arrows point to the different vessel size categories (long: white; medium: yellow; short: blue). (B) CD31+ vascular density was shown for each condition (Ctrl = 5, SDR = 5, uHDR = 5 brains). Data are presented as means and standard error of the means (SEM). Treatments were compared using ANOVA Tukey's post hoc test, SEM (*$P < .05$, **$P < .01$). (C) CD31+ structures are shown according to 3 vessel size categories, that is, long (elongation factor [EF]: >6), medium (EF: 3-6), and short (EF: 0-3), where each dot represents an average value of 10 analyzed regions of interest within one tissue. Horizontal lines represent means with SEM. Treatments were compared using unpaired 2-tailed Student's *t* test (*$P < .05$, **$P < .01$).

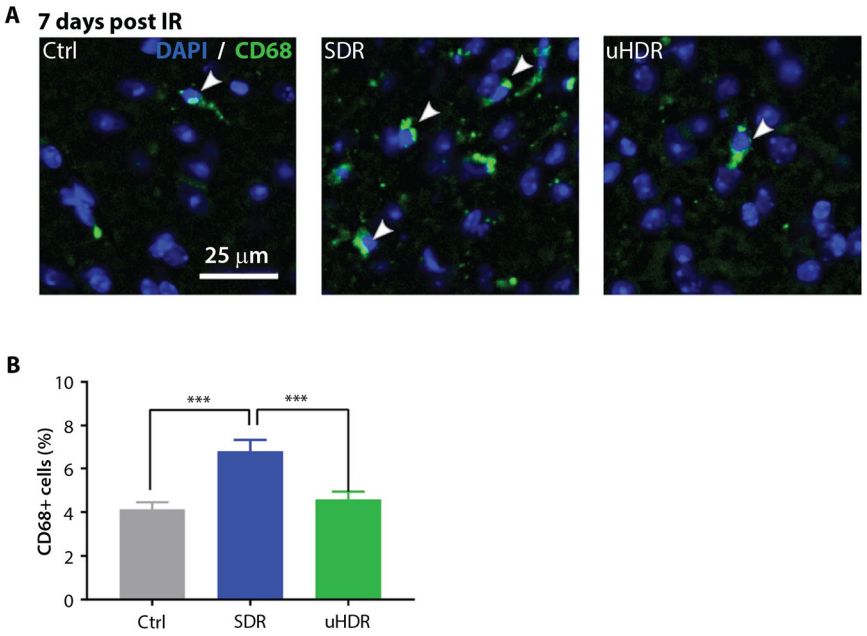

Fig. 4.

Standard dose rate (SDR) versus ultrahigh dose rate (uHDR) effects on inflammatory response. (A) Representative images (magnification 20 ×) of microglia/macrophages CD68− positive cells at 7 days post-irradiation of mouse brain cortex. Arrowheads indicate CD68-positive cells. (B) Quantification of CD68+ cells per analyzed area (~500 × 500 μm^2) at 7 days. Bars represent means with standard error of the means (SEM) (Ctrl = 5, SDR = 5, uHDR = 5 brains, 10 regions of interest per tissue section were analyzed). Treatments were compared using ANOVA Tukey's post hoc test, SEM (***$P < .005$).

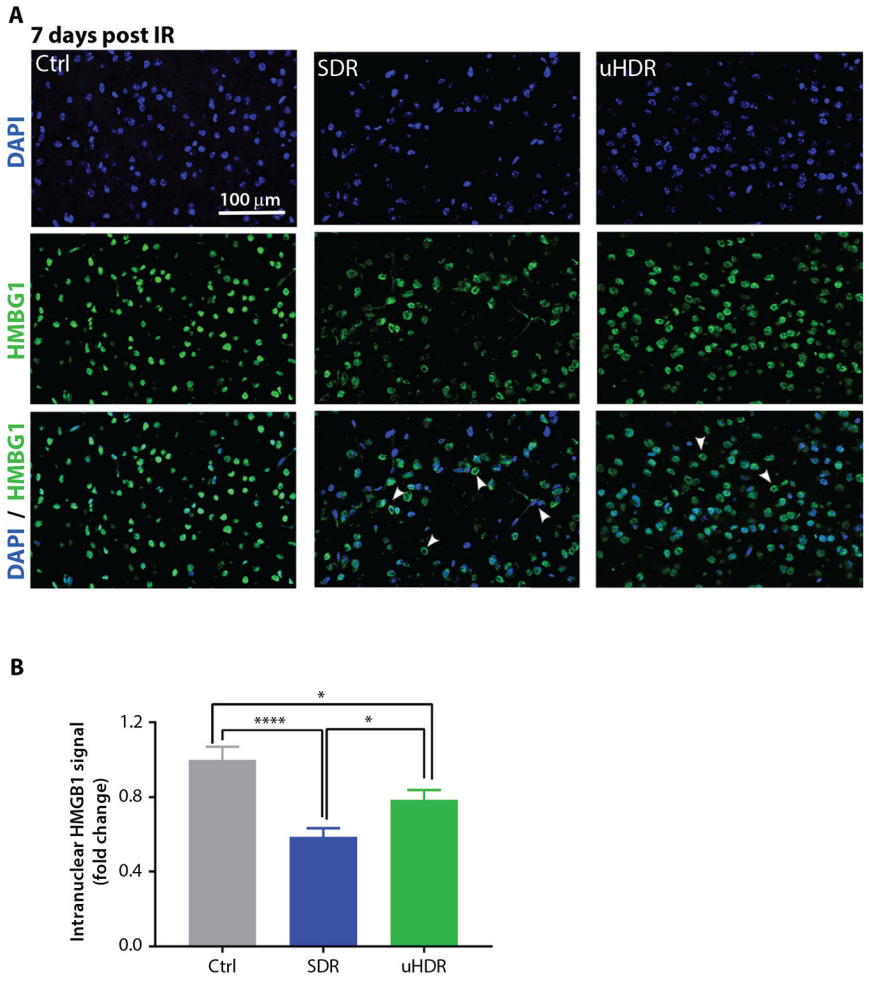

Fig. 5.

Standard dose rate (SDR) versus ultrahigh dose rate (uHDR) effects on HMGB1 expression. (A) Representative images of high mobility group box protein 1 (HMGB1) signal at 7 days postirradiation of mouse brain cortex (magnification 20 ×). Arrowheads point to the nuclei that have released HMGB1 to the cytoplasm. (B) Quantification of nuclear HMGB1 signal. Bars represent means with standard error of the means (SEM) (Ctrl = 5, SDR = 5, uHDR = 5 brains, 10 regions of interest per tissue section were analyzed). Treatments were compared using ANOVA Tukey's post hoc test, SEM (*$P < .05$; ****$P < .0001$).

Table 1

Irradiation settings, parameters, and dosimetric measurements for SDR and uHDR

	Dose (Gy)	Delivery time (s)	Interspill time (s)	Spill time (s)	Delivery mean dose rate (Gy/s)	Instant spill dose rate (Gy/s)
SDR	9.7	58	6.5	0.25	0.17	38.8
uHDR	9.6	0.08	-	0.08	120.0	120.0

Abbreviations: SDR = standard dose rate; uHDR = ultrahigh dose rate.